Received: 19 June 2023 | Revised: 11 August 2023 | Accepted: 17 August 2023

DOI: 10.1002/agt2.412

Aggregate WILEY

RESEARCH ARTICLE

Fluorogenic sensing of amorphous aggregates, amyloid fibers, and chaperone activity via a near-infrared aggregation-induced emission-active probe

Wei He[1] | **Yuanyuan Yang**[1] | **Yuhui Qian**[1] | **Zhuoyi Chen**[1] | **Yongxin Zheng**[1] | **Wenping Zhao**[1] | **Chenxu Yan**[2] | **Zhiqian Guo**[2] | **Shu Quan**[1,3]

[1]State Key Laboratory of Bioreactor Engineering, Shanghai Collaborative Innovation Center for Biomanufacturing (SCICB), East China University of Science and Technology, Shanghai, China

[2]Key Laboratory for Advanced Materials and Joint International Research Laboratory of Precision Chemistry and Molecular Engineering, Shanghai Key Laboratory of Functional Materials Chemistry, Frontiers Science Center for Materiobiology and Dynamic Chemistry, Institute of Fine Chemicals, School of Chemistry and Molecular Engineering, East China University of Science and Technology, Shanghai, China

[3]Shanghai Frontiers Science Center of Optogenetic Techniques for Cell Metabolism, East China University of Science and Technology, Shanghai, China

Correspondence
Wei He, State Key Laboratory of Bioreactor Engineering, East China University of Science and Technology, Shanghai Collaborative Innovation Center for Biomanufacturing (SCICB), Shanghai 200237, China.
Email:whe@mail.ecust.edu.cn

Shu Quan, Shanghai Frontiers Science Center of Optogenetic Techniques for Cell Metabolism, East China University of Science and Technology, Shanghai 200237, China.
Email:shuquan@ecust.edu.cn

Funding information
Natural Science Foundation of Shanghai, Grant/Award Number: 23ZR1415300; National Natural Science Foundation of China, Grant/Award Numbers: 32222049, 31661143021, 32171269, 32201043; National Key Research and Development Program of China, Grant/Award Number: 2022YFF1102900; Shanghai Frontier Science Center of Optogenetic Techniques for Cell Metabolism Shanghai Municipal Education Commission, Grant/Award Number: 2021Sci&Tech0328

Abstract

The presence of protein aggregates in numerous human diseases underscores the significance of detecting these aggregates to comprehend disease mechanisms and develop novel therapeutic approaches for combating these disorders. Despite the development of various biosensors and fluorescent probes that selectively target amyloid fibers or amorphous aggregates, there is still a lack of tools capable of simultaneously detecting both types of aggregates. Herein, we demonstrate the quantitative discernment of amorphous aggregates by QM-FN-SO_3, an aggregation-induced emission (AIE) probe initially designed for detecting amyloid fibers. This probe easily penetrates the membranes of the widely-used prokaryotic model organism *Escherichia coli*, enabling the visualization of both amorphous aggregates and amyloid fibers through near-infrared fluorescence. Notably, the probe exhibits sensitivity in distinguishing the varying aggregation propensities of proteins, regardless of whether they form amorphous aggregates or amyloid fibers in vivo. These properties contribute to the successful application of the QM-FN-SO_3 probe in the subsequent investigation of the antiaggregation activities of two outer membrane protein (OMP) chaperones, both in vitro and in their physiological environment. Overall, our work introduces a near-infrared fluorescent chemical probe that can quantitatively detect amyloid fibers and amorphous aggregates with high sensitivity in vitro and in vivo. Furthermore, it demonstrates the applicability of the probe in chaperone biology and its potential as a high-throughput screening tool for protein aggregation inhibitors and folding factors.

KEYWORDS
aggregation-induced emission, fluorescence, molecular chaperone, protein aggregation

1 | INTRODUCTION

Correct folding is essential for proteins to perform their intended physiological functions. Genetic mutations, alterations in folding conditions, and posttranslational modifications can divert protein folding toward misfolding, which often leads to aggregation.[1–3] To counteract this, a complex proteostasis network (PN) comprising molecular chaperones

and protein degradation machinery has evolved, aiming to assist folding, prevent misfolding, and degrade misfolded proteins.[4–6] However, when the level of protein misfolding overwhelms the regulatory capacity of the PN, protein aggregation occurs and contributes to the pathogenesis of numerous human diseases, such as peripheral amyloidosis, type II diabetes, cardiovascular diseases, and many neurodegenerative disorders.[7,8]

Detection and visualization of protein aggregates are crucial for both mechanistic understanding and the development of new therapeutic strategies for protein aggregation-related diseases. Several types of antibody- and aptamer-based probes have been devised for protein aggregation detection, contributing significantly to protein folding studies.[9–12] Nevertheless, the limited stability and susceptibility to denaturation of these probes have restricted their applications.[13] In contrast, fluorescent probes offer several advantages, including robustness, high sensitivity, and cost-effectiveness, making them an attractive avenue for protein aggregation research.[14,15]

Currently, the primary emphasis of chemical probes lies in targeting amyloid fibers. This preference is motivated by the strong association of amyloid fibers with dozens of human diseases, as well as their well-defined cross β-strand structures, which are ideal for structure-based probe design.[16–19] Examples include derivatives of the "gold standard" thioflavin, Congo red derivatives, and aggregation-induced emission (AIE) probes.[20–22] The AIE probes, in particular, have gained significant attention for overcoming the limitations of traditional amyloid probes, such as always-on properties and aggregation-caused quenching (ACQ) effect.[23] In a remarkable development, Zhang's group has rationally designed a series of AIE probes capable of detecting not only amyloid fibrils, but also previously invisible intermediate species (i.e., misfolded oligomers) and distinguishing them from mature amyloid fibers.[24,25] This breakthrough makes it possible to monitor the entire aggregation process of amyloid proteins in live cells.[26]

In contrast to the extensive focus on amyloid fibers, there has been relatively limited attention directed toward the development of fluorescent probes specifically targeting amorphous aggregates. These protein assemblies lack well-defined structures and arise from disordered or largely disordered protein compaction, making it challenging to identify specific binding sites and epitopes for fluorescent probes.[27–29] Amorphous aggregates encompass entities like inclusion bodies, which are frequently observed during protein overexpression. While historically considered generally non-toxic to cells, their presence is often linked to adverse effects, including the loss of function of the aggregated proteins and interference with the function and solubility of other proteins.[30] In contemporary research, mounting evidence indicates the widespread occurrence of amorphous aggregates in protein deposition-related diseases.[31] Notably, the same disease-related protein may exhibit the capability to form either amorphous aggregates or amyloid fibrils in different circumstances. For instance, β2-microglobulin, implicated in dialysis-related amyloidosis, can adopt either amyloid fibrils or amorphous aggregates, depending on the salt concentration.[29] Similarly, α-synuclein, related to Parkinson's disease (PD), can manifest both amorphous aggregates and amyloid fibers, influenced by factors such as amino acid mutations, diverse environmental conditions, and interactions with other molecules.[32]

Liu's group has successfully devised multiple AIE probes for the selective detection of amorphous aggregates through precise modulation of the viscosity and polarity sensitivity of the dicyanoisophorone (DCI) fluorophore, employing a typical donor-π-acceptor (D-p-A) structure.[33,34] Further analysis of the relationship between structure and fluorescence signal revealed that the presence of a dimethylaminophenylene group on the electron-donating end is crucial for recognizing amorphous aggregates and activating fluorescence.[33] Overall, these endeavors have yielded a range of probes, each specific to either amyloid or amorphous aggregates. However, there remains a gap for fluorescent probes with a broad sensitivity to both types of protein aggregates, applicable in both in vitro and in vivo settings. Because as aforementioned, some proteins can generate both amorphous aggregates and amyloid fibers, probes tailored exclusively for detecting either amorphous aggregates or amyloid fibrils could potentially overlook the formation of the alternative aggregation type by the same disease-associated protein under specific conditions. Such limitations may lead to misinterpretations in protein aggregation-related disease investigations. Developing dual-function probes would thus provide an expanded avenue for protein aggregation analysis and offer versatility in experimental design and application.

Herein, we test if the QM-FN-SO_3 fluorescent probe that we previously designed for amyloid fibers mapping in situ could also detect amorphous aggregates. We hypothesize that this is possible because the QM-FN-SO_3 fluorescent probe contains a typical D-p-A-structure and a dimethylaminophenylene group on the electron-donating end similar to the amorphous aggregates-specific probes developed by Liu's group (Figure 1A).[35] Our results show that QM-FN-SO_3 can quantitatively detect a set of model amorphous aggregates and monitor the progression of their formation in vitro. In addition, we demonstrate that QM-FN-SO_3 exhibits excellent penetration properties, allowing it to traverse both the outer and inner membranes of the widely-utilized prokaryotic protein expression host *E. coli* BL21(DE3) and illuminate both amyloid fibers and amorphous aggregations in vivo (Figure 1B). Remarkably, the AIE fluorescence of QM-FN-SO_3 can sensitively report the different aggregation propensities of proteins, irrespective of whether they form amorphous aggregates or amyloid fibers in vivo. These findings encouraged us to test whether QM-FN-SO_3 can be used to measure chaperone activities. Through QM-FN-SO_3 fluorescence assays, we assessed the antiaggregation activity of two OMP chaperones, SurA and Skp, toward their physiological substrate outer membrane protein X (OmpX).[36–38] We found that SurA exhibits more pronounced chaperone activity in vivo than Skp, despite being less efficient in inhibiting OmpX aggregation in vitro. This is consistent with SurA's established role as the principal molecular chaperone involved in outer membrane biogenesis and emphasizes the divergence of chaperone activity when assayed in vitro and in vivo.[39,40] Taken together, our study presents a valuable chemical fluorescent tool for quantitatively detecting amyloid fibers and amorphous aggregates in vitro and in vivo, and highlights the tool's efficiency in characterizing chaperone activity and its potential application

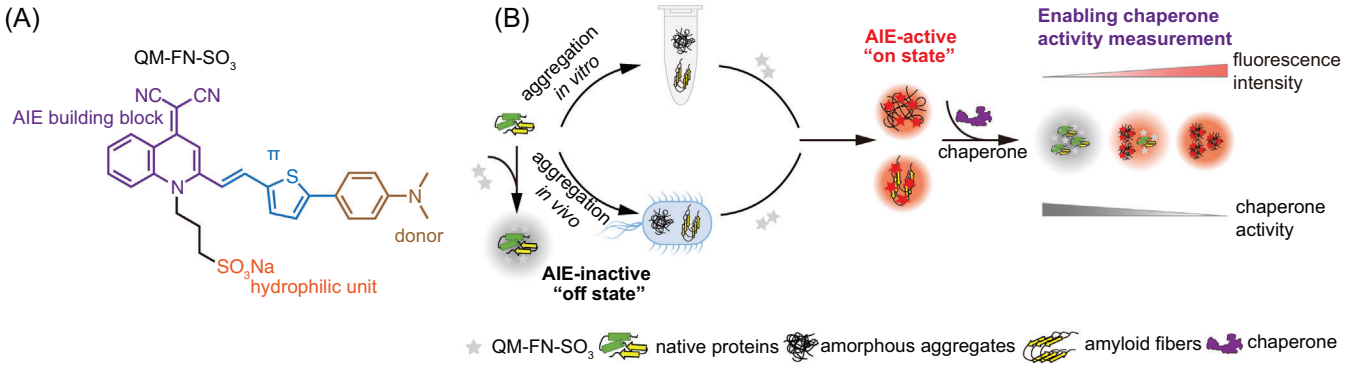

FIGURE 1 **Aggregate detection via the near-infrared (NIR) AIE-active probe, QM-FN-SO$_3$.** (A) QM-FN-SO$_3$ structure. (B) Schematic illustrations of the applications of the QM-FN-SO$_3$ probe in detecting amorphous aggregates, amyloid fibers, and chaperone activity both in vitro and in vivo.

as a selection tool for drugs inhibiting disease-related protein aggregation.

2 | RESULTS AND DISCUSSION

2.1 | Quantitative detection of amorphous aggregates with the QM-FN-SO$_3$ probe

To test whether QM-FN-SO$_3$ can detect amorphous aggregates, we monitored the fluorescence spectra of QM-FN-SO$_3$ in the presence and absence of various concentrations of heat-aggregated malate dehydrogenase (MDH). QM-FN-SO$_3$ was nonemissive in the absence of MDH aggregates or in the presence of native MDH, whereas showing bright near-infrared (NIR) fluorescence in the presence of MDH aggregates with a maximal emission wavelength (em_{max}) at 680 nm (Figure 2A,B). Moreover, the QM-FN-SO$_3$ fluorescence intensities showed a good linear correlation with the concentrations of MDH aggregates within the micro molar range (Figure 2C). Similar behavior of QM-FN-SO$_3$ was observed when assayed with chemically-aggregated α-lactalbumin (α-LA) (Figure 2D).

We then examined the aggregation kinetics of heat-treated MDH and chemically-treated α-LA by monitoring the increase in QM-FN-SO$_3$ fluorescence (Figure 2E,F) and compared their curves with those obtained by monitoring light scattering, a traditional method for detecting protein aggregation. We found that although the aggregation curves monitored by the two methods did not overlap, both methods revealed similar times required to reach maximal aggregation, demonstrating the capability of the QM-FN-SO$_3$ probe to monitor protein aggregation process (Figure S1A,B). Notably, we found that the aggregation curve of α-LA monitored by QM-FN-SO$_3$ fluorescence displayed significant signals at the early phase of aggregation, whereas the curve determined by the light scattering method showed only minimal signals at the same stage (Figure S1B). We excluded the possibility that the early fluorescence signals were caused by QM-FN-SO$_3$ itself (Figure S1D) and speculated that these signals might be activated by misfolded oligomers that were too small to be detected by light scattering. However, this effect was not seen for MDH aggregates and thus might be protein-specific (Figure S1A,C). Nevertheless, for denatured MDH that aggregates rapidly and quickly reaches the detection limit of light scattering, the QM-FN-SO$_3$ probe can still give quantitative monitoring of these processes.

To further test the generalizability of the QM-FN-SO$_3$ probe in detecting amorphous aggregates, we analyzed its ability to quantify chemically-denatured aggregates of OmpX as well as heat-aggregated whole cell lysates of *E. coli*. Similarly, we were able to monitor aggregation kinetics and obtain aggregate concentration-dependent fluorescence signals for these samples (Figures S2, S3). Quantification of the OmpX aggregates allowed us to obtain the limit of detection (LOD) of the QM-FN-SO$_3$ probe on this protein aggregate, which is in the nano molar range (Figure S2). These results collectively demonstrated the superior sensitivity and generalizability of the QM-FN-SO$_3$ probe to detect amorphous aggregates.

2.2 | Rapid and robust illumination of amorphous aggregates in vivo

We previously showed that QM-FN-SO$_3$ had significant blood-brain barrier (BBB) penetrability, allowing it to bind and fluorescently label amyloid beta peptide (Aβ) plaques in living mice.[35] This encouraged us to investigate whether this probe can traverse the densely packed outer and inner membranes of *E. coli* and thus be used to visualize protein aggregates in prokaryotic systems. To this end, we first tested whether the QM-FN-SO$_3$ probe could penetrate the outer membrane of *E. coli* and illuminate the periplasmic protein aggregates in heat shocked *E. coli* MG1655 *ΔdegP* strain. DegP is a periplasmic protease that degrades unfolded proteins and deletion of the *degP* gene leads to aggregation formation in the periplasm of *E. coli* under heat shock conditions.[41,42] As anticipated, we found that the QM-FN-SO$_3$ fluorescence of the *E. coli* MG1655 *ΔdegP* strain increased throughout the heat shock process, whereas the wild-type strain displayed a slight increase in QM-FN-SO$_3$ fluorescence in the first hour of the heat shock, but returned to background fluorescence as the heat shock time was extended (Figure 3A). This indicates that the QM-FN-SO$_3$ probe is able to penetrate the outer membrane of *E. coli* and reveal protein aggregation within the periplasm.

Next, we investigated whether the QM-FN-SO$_3$ probe could traverse the inner membrane of *E. coli* and detect cytoplasmic protein aggregation. To achieve this, we overexpressed OmpX in the cytoplasm of the bacteria strain

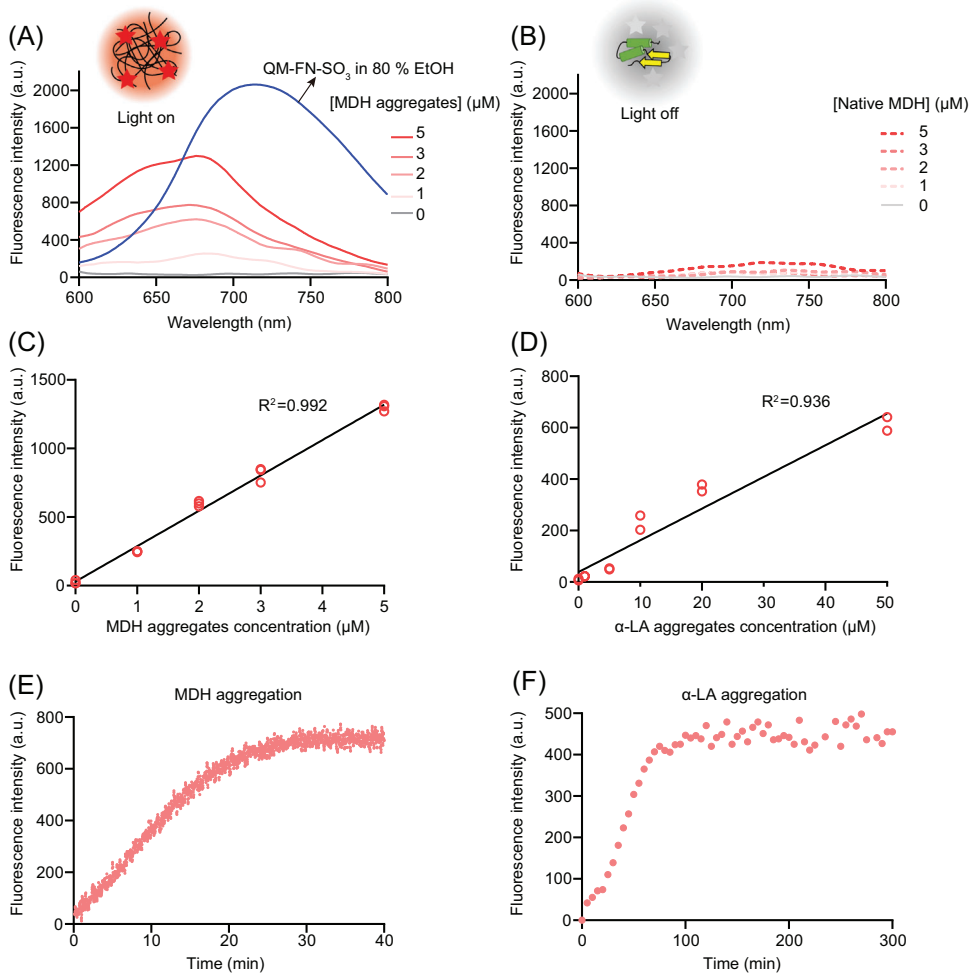

FIGURE 2 **QM-FN-SO_3 enables the quantitative detection of amorphous aggregates**. (A) Fluorescence spectra of 1 μM QM-FN-SO_3 in the presence or absence of various amounts of heat-aggregated malate dehydrogenase (MDH). QM-FN-SO_3 is non-emissive in water while illuminating near-infrared (NIR) fluorescence with a maximal wavelength at 720 nm in the presence of 80% ethanol solution. QM-FN-SO_3 em_{max} shifted to 680 nm in the presence of MDH aggregates. (B) Fluorescence spectra of 1 μM QM-FN-SO_3 in the presence or absence of various concentrations of native MDH. (C-D) Correlation analyses between the aggregates concentrations of MDH (C) or α-lactalbumin (α-LA) (D) and the corresponding QM-FN-SO_3 fluorescence intensities. (E and F) Aggregation curves of 2 μM heat-treated MDH (E) or 50 μM DTT-treated α-LA (F) in the presence of 1 μM QM-FN-SO_3, as monitored by QM-FN-SO_3 fluorescence. The fluorescence intensities in C-F were measured with the excitation and emission wavelengths at 500 and 680 nm, respectively. For A, B, E, and F, representative curves of three independent experiments are shown. For C and D, individual data points (circles) of 2–4 independent measurements are shown.

BL21(DE3) and measured the QM-FN-SO_3 fluorescence according to the procedure in Figure 3B. It is well-established that OmpX overexpressed in the cytoplasm forms amorphous aggregates.[43] As expected, we found that cells overexpressing OmpX displayed bright fluorescence in the presence of the QM-FN-SO_3 probe, whereas cells carrying an empty vector or overexpressing the soluble chaperone protein Spy, which has a molecular weight comparable to OmpX, displayed negligible QM-FN-SO_3 fluorescence (Figure 3C). Super-resolution microscopic images revealed predominant colocalization of the QM-FN-SO_3 probe with dark spots distributed at the cell poles or associated with the cell membrane, presumably representing OmpX inclusion bodies (Figure 3D).

The signal of QM-FN-SO_3 bound to OmpX aggregates was robust, becoming immediately visible upon the addition of QM-FN-SO_3 into the culture medium or phosphate-buffered saline (PBS) buffer and reaching its peak intensity within approximately 10 min (Figure S4A,C). Furthermore, the fluorescence intensity remained consistent regardless of the presence or absence of free QM-FN-SO_3 probe (Figure S4B–D). Taken together, these results suggest that the QM-FN-SO_3 probe can efficiently penetrate both the bacterial outer and inner membranes, resulting in the accurate and robust visualization of amorphous aggregates in vivo.

2.3 | Discriminating the aggregation propensities of proteins forming either amorphous aggregates or amyloid fibers in vivo

We further investigated the sensitivity of QM-FN-SO_3 fluorescence in distinguishing the varying aggregation propensities of proteins that form amorphous aggregates. To examine this, we measured the QM-FN-SO_3 fluorescence in cells overexpressing either the wild-type immunity protein 7 (Im7) or its mutants with defined thermostability.[44] Proteins with lower thermostability generally exhibit higher aggregation propensities when expressed in vivo.[45] Consistent with previous observations, we found that the less stable Im7 mutants formed more aggregates in cells (Figure S5A). In addition, the QM-FN-SO_3 fluorescence readout

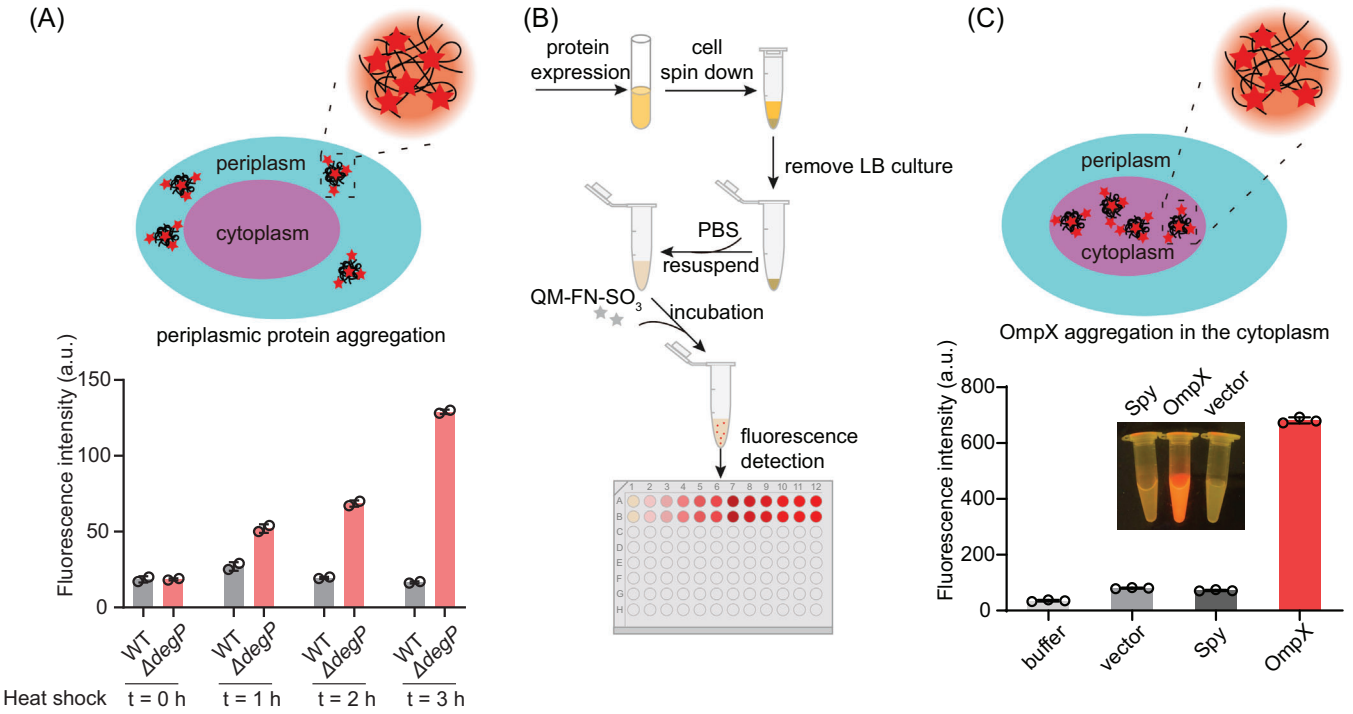

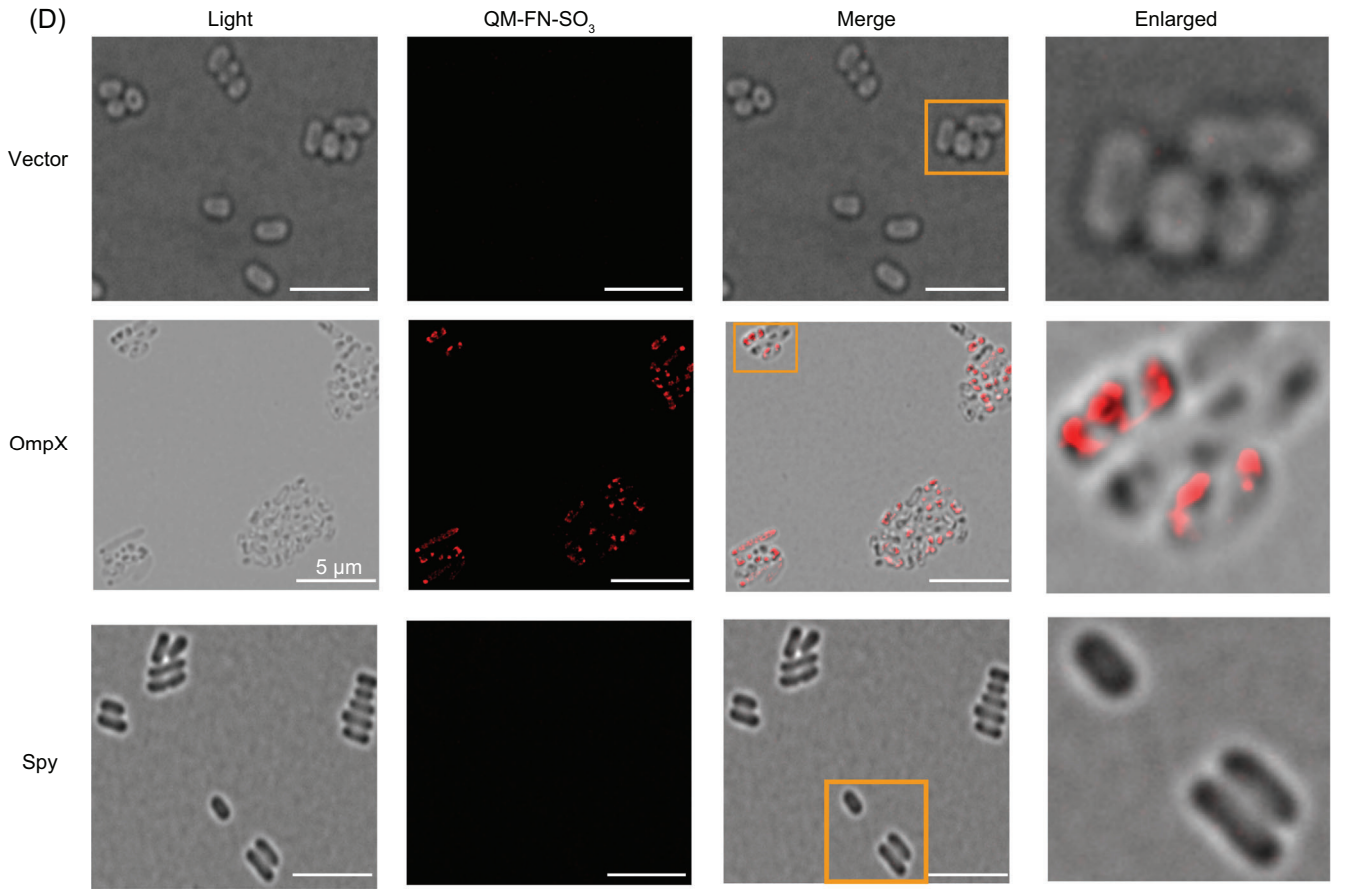

FIGURE 3 **Detection of amorphous aggregates in vivo by the QM-FN-SO_3 probe**. (A) Detection of periplasmic protein aggregation using QM-FN-SO_3 fluorescence. *Escherichia coli* MG1655 wild type and Δ*degP* strains were subjected to heat shock treatment (43°C). At the indicated time points, cells were harvested, adjusted to an optical density of 5 OD/mL, and incubated with 10 μM QM-FN-SO_3 probe for 10 min prior to fluorescence measurements. Individual data points (circles) and mean ± SD ($n = 2$) are shown. A schematic illustration of periplasmic protein aggregates bound by the QM-FN-SO_3 probe is shown on the upper panel. (B) Schematic representation of the amorphous aggregates detection steps in *E. coli*. (C) QM-FN-SO_3 fluorescence of *E. coli* cells expressing either the empty vector, the aggregation-prone OmpX, or the soluble chaperone protein Spy in the cytoplasm. Individual data points (circles) and mean ± SD ($n = 3$) are shown. A schematic illustration of intracellular OmpX aggregates bound by the QM-FN-SO_3 probe is shown on the upper panel. (D) Structured light illumination microscopy (SIM) images of OmpX- or Spy-expressing *E. coli* labeled with the QM-FN-SO_3 probe. Cells containing the empty vector were used as a control. Cells analyzed in (C) and (D) were induced for protein expression for 2.5 h. QM-FN-SO_3, quinoline-malononitrile-thiophene-(dimethylamino)phenylsulfonate; SET, Su(var)3-9, Enhancer-of-zeste, and Trithorax.

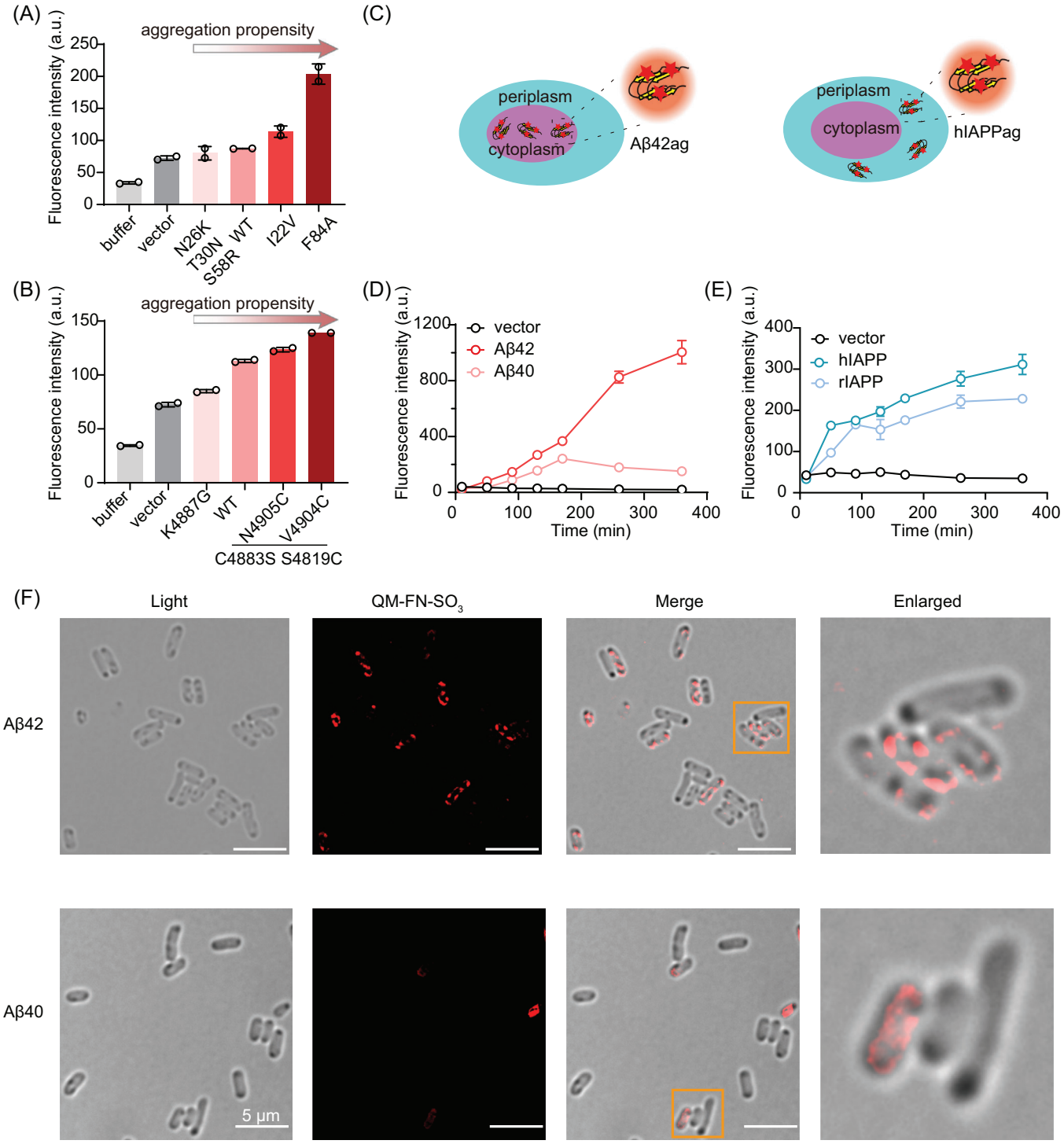

FIGURE 4 **Distinguishing the different aggregation propensities of model proteins in vivo with QM-FN-SO_3.** (A and B) QM-FN-SO_3 fluorescence intensities of *Escherichia coli* expressing Im7 mutants (A) or MLL3 SET domain mutants (B). Individual data points (circles) and mean ± SD ($n = 2$) are shown. Cells used to detect QM-FN-SO_3 fluorescence were induced for protein expression for 4 h. (C) Illustrations of the detections of cytoplasmically-expressed Aβ42 aggregates or periplasmically-expressed hIAPP aggregates by the QM-FN-SO_3 probe. (D and E) Aggregation processes of the Aβ40 and Aβ42 pair (D) and the hIAPP and rIAPP pair (E) in *E. coli* monitored by the QM-FN-SO_3 fluorescence (mean ± SD, $n = 2$). (F) Structured light illumination microscopy (SIM) images of *E. coli* expressing the indicated proteins labeled with the QM-FN-SO_3 probe. Cells in (F) were induced for protein expression for 4 h before analysis.

was well correlated with the aggregation propensity of Im7 wild type and its mutants (Figure 4A, Figure S5B). Similar results were observed in cells expressing variants of the histone H3K4 methyltransferase MLL3 SET domain, with the most aggregation-prone mutant MLL3 SET C4883S S4819C V4904C being almost completely insoluble and exhibited the highest QM-FN-SO_3 fluorescence (Figure 4B, Figure S5C, D).

The capability of the QM-FN-SO_3 probe to quantitatively detect Alzheimer's disease-related amyloid beta peptide 42 (Aβ42) fibers has been previously demonstrated.[35] Thus, we reasoned that this probe might also be able to discriminate the aggregation propensities of amyloidogenic proteins. We picked the Aβ42 and the less aggregation-prone Aβ40 peptide as a test pair, as well as human islet amyloid polypeptide (hIAPP), a 37-residue polypeptide associated with type II

diabetes mellitus, and its nonamyloidogenic counterpart, rat islet amyloid polypeptide (rIAPP).[46–49]

We first demostrated that the QM-FN-SO_3 probe performed effectively in characterizing the aggregation process of various concentrations of hIAPP in vitro, achieving a LOD value of 230 nM (Figure S6A,B). Notably, this value is three times lower than that of thioflavin T (ThT), which not only displayed higher background fluorescence but also showed a lesser fold change in its fluorescence signals when bound to different amounts of hIAPP fibers (Figure S6C,D). While the absorption spectra of QM-FN-SO_3 displayed a comparable red-shift when bound to hIAPP fibers and OmpX aggregates, the quantum yield of the probe for hIAPP fibers was marginally higher than that for OmpX aggregates (measured at equivalent concentrations) (Figure S7). This observation suggests a more constrained microenvironment within hIAPP fibers in contrast to OmpX aggregates. Super-resolution imaging further revealed that hIAPP fibers adopt expansive interlacing lamellae, whereas OmpX assumes discrete, isolated punctate structures (Figure S8).

Since hIAPP contains a disulfide bond which plays a role in amyloid formation, we then expressed hIAPP and rIAPP in the oxidative bacterial periplasm to allow disulfide bond formation, while expressing Aβ40 and Aβ42 in the cytoplasm (Figure 4C).[50] Formation of the Aβ42 and hIAPP amyloid fibers was independently demonstrated by ThT fluorescence and circular dichroism (CD) assays (Figure S9A–C). Incubating the pellet fractions of cells expressing Aβ42 or hIAPP with QM-FN-SO_3 produced bright NIR fluorescence with the em_{max} around 680 nm, illustrating the fluorescence activation property of QM-FN-SO_3 in the presence of amyloid fibers. Notably, QM-FN-SO_3 showed a significantly lower cellular fluorescence background than ThT, highlighting its advantages for in vivo detection of amyloid fibers (Figure S9A,D).

We subsequently used QM-FN-SO_3 to monitor the in vivo amyloidogenic process of the Aβ40 and Aβ42 pair as well as the hIAPP and rIAPP pair. We found that although cells expressing all these peptides exhibited QM-FN-SO_3 fluorescence (Figure 4D,E), cells expressing Aβ42 or hIAPP showed higher fluorescence intensity than cells expressing their low-aggregation propensity counterpart peptides (Aβ40 or rIAPP) throughout the entire expression period (Figure 4D,E). These findings were further supported by fluorescence images (Figure 4F and Figure S10). In addition, we observed a correlation between the aggregation propensity of these amyloid peptides and their toxicity to the host cells (Figure S9E,F). Taken together, these results strongly support that the QM-FN-SO_3 probe is a potent fluorescent tool capable of monitoring and distinguishing the different aggregation propensities of both amorphous-type and amyloid-type aggregates in vivo.

2.4 | Applying the QM-FN-SO_3 probe to characterize chaperone activities both in vitro and in vivo

The ability of the QM-FN-SO_3 probe to distinguish various protein aggregation levels promoted us to investigate its application in chaperone activity assessment. To examine this, we tested the anti-aggregation activity of the periplasmic chaperone SurA and Skp toward their physiological substrate, OmpX, by QM-FN-SO_3 fluorescence assays.[40] We chemically denatured OmpX and monitored its aggregation process under refolding conditions in the presence and absence of various concentrations of SurA or Skp. We found that the QM-FN-SO_3 fluorescence intensity of OmpX decreased with increasing concentrations of SurA or Skp, with Skp being more competent in decreasing the fluorescence signals than SurA (Figure 5A). Moreover, these aggregation curves shared nearly the same trend as those curves monitored by light scattering. The equilibrated QM-FN-SO_3 fluorescence intensities of OmpX in the presence and absence of various concentrations of SurA or Skp correlated quite well with the corresponding light scattering signals (Figure 5B,C). These results suggest that the QM-FN-SO_3 probe was capable of indicating and distinguishing the different anti-aggregation activities of chaperones in vitro.

Many studies have demonstrated a higher in vitro anti-aggregation activity of Skp on OMPs compared to SurA.[51] However, it is well-recognized that SurA plays the major role in maintaining OMPs in a folding-competent state and escorting them for outer membrane insertion, while Skp functions in a parallel manner to rescue OMPs that "fall off" the SurA pathway.[40] Despite the significance of these findings, the lack of suitable tools has hindered the direct determination of in vivo anti-aggregation activities of SurA and Skp. Previous studies have predominantly relied on phenotypic assays, proteomics approaches, and western blotting methods to draw conclusion in this regard.[51] To directly compare the activity of the two chaperones, we co-expressed SurA or Skp with OmpX in the bacterial periplasm and monitored the aggregation levels of OmpX of the resulting strains using QM-FN-SO_3 fluorescence (Figure 5D). We found that overexpression of OmpX in the periplasm led to severe aggregation as reflected by the high QM-FN-SO_3 fluorescence intensity and induced toxicity to the host strain, while co-expression of SurA strongly decreased aggregation and rescued strain growth (Figure 5E–G). In contrast to the in vitro observations, co-expression of Skp only inhibited OmpX aggregation at the early stage and did not improve bacterial growth (Figure 5E–G), despite the fact that the steady-state level of Skp was detected to be similar to that of SurA (Figure S11).

SurA functions as a dedicated chaperone for OMPs by recognizing the characteristic Ar-X-Ar motif (where Ar signifies an aromatic residue and X can be any amino acid) located at the C-terminus of OMPs.[51] In contrast, Skp demonstrates a promiscuous substrate recognition profile, also displaying chaperone activity toward various non-OMP substrates.[51] Therefore, we hypothesize that the lower in vivo chaperone activity of Skp toward OmpX observed above might arise from Skp's promiscuous nature, leading to its sequestration by other periplasmic proteins and consequently reducing the number of Skp molecules available to protect OmpX. To examine this, we substituted the buffer in the OmpX refolding experiment with periplasmic extracts from the BL21(DE3) strain and repeated the experiment shown in Figure 5A (Figure S12A). At low chaperone concentration, we found that SurA performed better than Skp, which is consistent with the in vivo results (Figure S12B,C). However, as chaperone concentration increased, Skp outperformed SurA (Figure S12B,C). These results support, at least in part, our

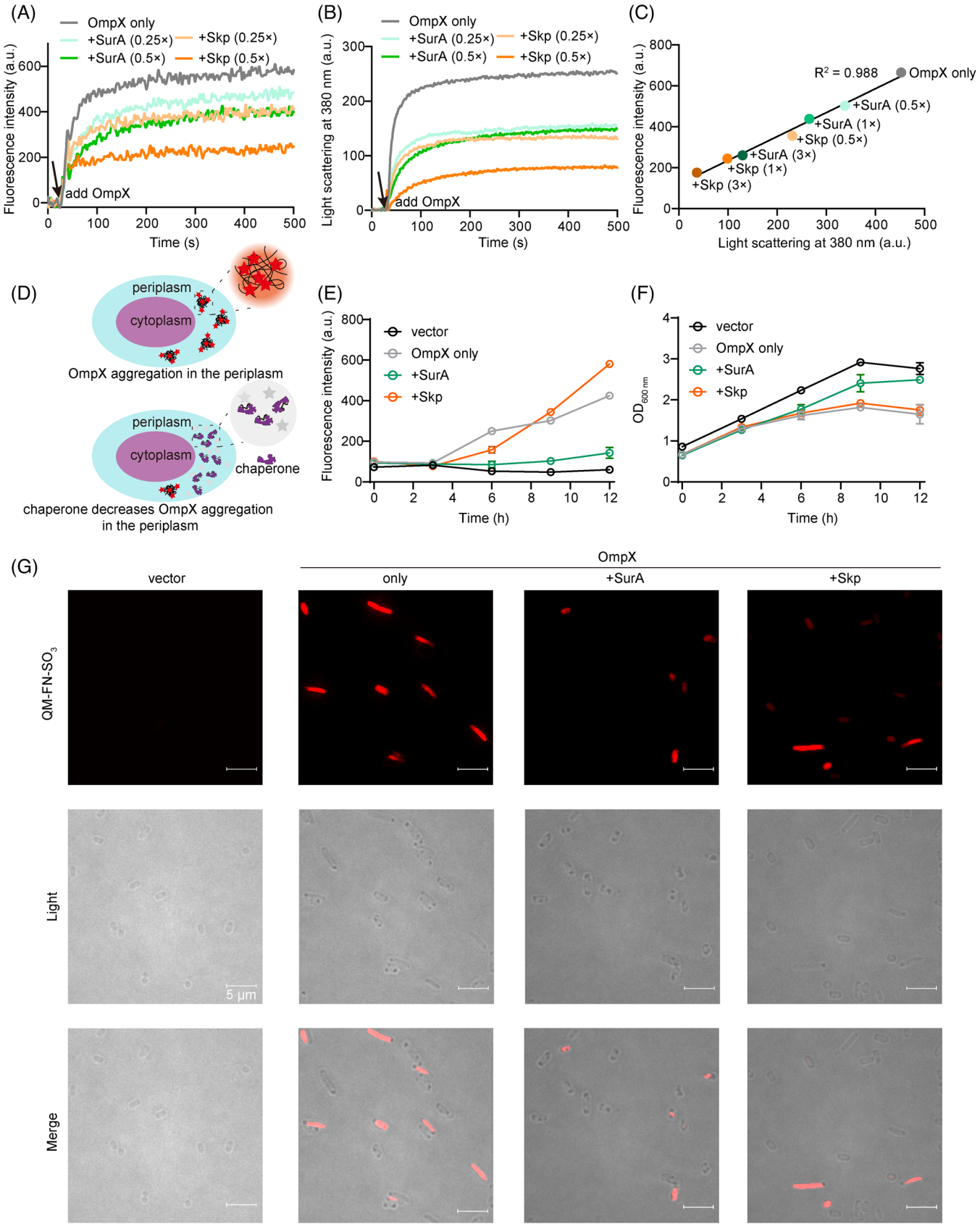

FIGURE 5 **Assessment of in vitro and in vivo chaperone activity through the QM-FN-SO_3 fluorescence detection**. (A and B) Aggregation curves of 1.5 μM urea-denatured OmpX with varying concentrations of SurA and Skp, monitored by QM-FN-SO_3 fluorescence (A) or light scattering (B). Representative curves from three independent experiments are presented. (C) Correlation analysis between QM-FN-SO_3 fluorescence intensities and light scattering signals of OmpX aggregates in the presence and absence of SurA and Skp at various concentrations. (D) Illustrations of QM-FN-SO_3 fluorescence detection of periplasmically-expressed OmpX aggregates in the presence and absence of chaperones. (E) Aggregation kinetics of periplasmically-expressed OmpX with or without co-expression of SurA or Skp, monitored by QM-FN-SO_3 fluorescence (mean ± SD, $n = 2$). (F) Growth curves of *E. coli* after induction of the indicated proteins (mean ± SD, n = 2). (G) Fluorescence micrographs of *E. coli* expressing the indicated proteins labeled with the QM-FN-SO_3 probe. Cells in (G) were induced for protein expression for 6 h before imaging.

hypothesis and offer insight into the higher in vitro yet diminished in vivo chaperone activity of Skp in comparison to SurA. Taken together, these results underscore the divergence between chaperone activity in vitro and in vivo and more importantly highlight QM-FN-SO_3's potency as a powerful tool in chaperone biology.

3 | CONCLUSIONS

In this study, we have demonstrated the versatility of the AIE fluorescent probe QM-FN-SO_3 for the quantitative and sensitive detection of both amorphous aggregates and amyloid fibers. A reliable probe requires good photostability. The QM-FN-SO_3 probe retained 60% of its original absorbance at 424 nm after continuous illumination (50 W) for 20 min, and exhibited enhanced photostability when bound to OmpX aggregates or hIAPP fibers (maintaining over 90% of the original absorbance) (Figure S13).

The remarkable penetration ability of QM-FN-SO_3 allowed it to traverse the dense double membranes of the commonly used model organism *E. coli*, enabling real-time monitoring of protein aggregation in vivo. The excellent photostability of the QM-FN-SO_3 probe confers it with the capability to be used for super-resolution microscopy. In addition, the probe was able to distinguish the different aggregation propensities of proteins regardless of whether they form amorphous aggregates or amyloid fibers in *E. coli*, making it an attractive tool to evaluate changes of protein aggregation in the presence and absence of folding factors. By co-expressing the aggregation-prone outer membrane protein OmpX and its physiological chaperone SurA and Skp, we demonstrated that the major outer membrane protein chaperone SurA was more capable of inhibiting OmpX aggregation in a physiological environment than Skp, despite Skp displaying higher anti-aggregation activity in vitro.

To broaden the scope of probe application to mammalian cells, we further tested if the QM-FN-SO_3 probe could detect protein aggregation in HEK 293T cells treated by heat shock or proteasome inhibition (by adding MG 132). Encouragingly, we observed elevated QM-FN-SO_3 fluorescence in stressed cells compared to untreated cells (Figure S14A,B). Moreover, fluorescence imaging revealed that the QM-FN-SO_3 probe could detect protein aggregates within both the cytosol and nucleus (Figure S14C). These findings strongly endorse the suitability of the QM-FN-SO_3 probe for use in mammalian systems and propose a promising future direction for its application in investigating physiological chaperone activity with mammalian cells and potentially even animal models.

While the QM-FN-SO_3 probe exhibits broad sensitivity toward both amyloid and amorphous-type protein aggregates, it is important to acknowledge the necessity for additional specific probes to accurately discern whether a given protein forms amyloid or amorphous aggregates. For example, after detecting aggregation using QM-FN-SO_3, researchers can employ amyloid-specific probes like ThT or bis(triphenylphosphonium) tetraphenylethene (TPE-TPP), in combination with the dicyanoisophorone (DCI) AIEgen-based amorphous aggregates-specific probe B6, for a more precise differentiation of aggregation types.[33,52] In conclusion, our work extends the application of the AIE fluorescent probe QM-FN-SO_3 for the quantitative and sensitive detection of amorphous aggregates and highlights its ability to facilitate the real-time monitoring and visualization of both amorphous aggregates and amyloid fibers in vitro and in vivo, suggesting its potential as a selection tool for protein aggregation inhibitors and folding factors.

4 | EXPERIMENTAL SECTION

4.1 | Materials

MDH from pig heart mitochondria and α-lactalbumin (α-LA; Type III from bovine milk) were purchased from Roche and Sigma-Aldrich, respectively. The QM-FN-SO_3 probe was synthesized as previously described.[53] Proteins SurA, Skp, and OmpX were expressed and purified from *E. coli* BL21(DE3), while Aβ42 and hIAPP were synthesized from SynPeptide Co. Ltd. Other chemical reagents were purchased from Sangon Biotech (Shanghai) Co. Ltd. All strains and plasmids used were from laboratory stock or constructed in this work, and are shown in Table 1.

4.2 | Amorphous aggregate detection in vitro

For MDH aggregate preparation, final concentrations of 1, 2, 3, and 5 μM MDH were incubated in a 40 mM HEPES-KOH buffer (pH = 7.5) at 60°C for 30 min to achieve complete aggregation. For α-LA aggregate preparation, 20 mM DTT was added to various concentrations of α-LA (1, 5, 10, 20, 50 μM) in a 50 mM NaP, 100 mM NaCl, 5 mM EDTA buffer (pH = 6.9) to trigger α-LA aggregation. For aggregate detection, 1 μM of the QM-FN-SO_3 probe was added, and the resulting activated fluorescence was detected using a Lumina Fluorescence Spectrometer (Thermo Fisher Scientific) with excitation and emission wavelengths set at 500 and 680 nm, respectively.

For aggregation curve assessment, 2 μM MDH was incubated in a 40 mM HEPES-KOH buffer (pH = 7.5) at 43°C while 20 μM α-LA was mixed with 20 mM DTT in a 50 mM NaP, 100 mM NaCl, and 5 mM EDTA buffer (pH = 6.9) to initiate aggregation. For OmpX, 1 mM OmpX stock in 50 mM NaP, 100 mM NaCl, 8 M urea buffer (pH = 7.0) was diluted to various concentrations (0.125, 0.5, 1, 2, 4, 8 μM) in a urea-free buffer to initiate aggregation. For hIAPP, 1 mg hIAPP protein powder was dissolved in 1 mL hexafluoroisopropanol (HFIP), followed by a sonication step to solubilize the pre-formed aggregates. Subsequently, soluble fractions of hIAPP were separated and subjected to freeze-drying for eliminating the HFIP solvent. The resulting frozen powder was then dissolved in ddH_2O and immediately diluted into a 50 mM Tris-HCl, 0.2 mM EDTA buffer (pH = 7.35) to final concentrations of 1, 5, 10, 20, 50 μM to trigger hIAPP aggregation. Time-dependent fluorescence signals in the presence of 1 μM QM-FN-SO_3 probe (ex = 500 nm, em = 680 nm) or 20 μM ThT (ex = 445 nm, em = 485 nm), as well as light scattering signals at 380 nm were recorded using a Lumina Fluorescence Spectrometer equipped with a Peltier temperature controller or a Synergy HTX Multi-Mode Microplate Reader (BioTeK).

TABLE 1 Strains and plasmids used in this work.

Strains and plasmids	Genotype and relevant description	Source or reference number
Escherichia coli strains		
BL21(DE3)	F$^-$ *ompT gal dcm lon hsdS$_B$*($r_B^-m_B^-$) λ(DE3 [*lacI lacUV5-T7p07 ind1 sam7 nin5*]) [*malB*$^+$]$_{K\text{-}12}$(λ^S)	Lab stock
Plasmids		
pET28b(+)	Kan^r; for inducible production of recombinant protein in *E. coli*; used as a vector only control for QM-FN-SO_3 fluorescence detection in vivo	Lab stock
pET28b(+)-HisSUMO-*surA*	Kan^r; for purification of SurA from *E. coli*	Lab stock
pET28b(+)-HisSUMO-*skp*	Kan^r; for purification of Skp from *E. coli*	[56]
pET28b(+)-His-*ompX*	Kan^r; for purification of OmpX from *E. coli*; used in the in vitro chaperone activity assay by the QM-FN-SO_3 probe	[56]
pET28b(+)-*ompX*	Kan^r; for cytoplamically expression of OmpX from *E. coli*; used in the in vivo QM-FN-SO_3 fluorescence detection	[56]
pET28b(+)-*spy*	Kan^r; for cytoplamically expression of Spy from *E. coli*; used as a control for QM-FN-SO_3 fluorescence detection in vivo	[56]
pET28b(+)-HisSUMO-*im7 WT*	Kan^r; for expression of Im7 WT from *E. coli*; used in the in vivo QM-FN-SO_3 fluorescence detection	[57]
pET28b(+)-HisSUMO-*im7 I22V*	Kan^r; for expression of Im7 I22V from *E. coli*; used in the in vivo QM-FN-SO_3 fluorescence detection	This study
pET28b(+)-HisSUMO-*im7 N26K T30N S58R*	Kan^r; for expression of Im7 N26K T30N S58R from *E. coli*; used in the in vivo QM-FN-SO_3 fluorescence detection	This study
pET28b(+)-HisSUMO-*im7 F84A*	Kan^r; for expression of Im7 F84A from *E. coli*; used in the in vivo QM-FN-SO_3 fluorescence detection	This study
pET28b(+)-HisSUMO-*mll3$_{SET}$ WT*	Kan^r; for expression of MLL3$_{SET}$ WT from *E. coli*; used in the in vivo QM-FN-SO_3 fluorescence detection	[58]
pET28b(+)-HisSUMO-*mll3$_{SET}$ K4887G*	Kan^r; for expression of MLL3$_{SET}$ K4887G from *E. coli*; used in the in vivo QM-FN-SO_3 fluorescence detection	This study
pET28b(+)-HisSUMO-*mll3$_{SET}$ S3819C C4883S V4904C*	Kan^r; for expression of MLL3$_{SET}$ S3819C C4883S V4904C from *E. coli*; used in the in vivo QM-FN-SO_3 fluorescence detection	This study
pET28b(+)-HisSUMO-*mll3$_{SET}$ S3819C C4883S N4905C*	Kan^r; for expression of MLL3$_{SET}$ S3819C C4883S N4905C from *E. coli*; used in the in vivo QM-FN-SO_3 fluorescence detection	This study
pET28b(+)-*aβ40*	Kan^r; for cytoplamically expression of Aβ40 from *E. coli*; used in the in vivo QM-FN-SO_3 fluorescence detection	This study
pET28b(+)-*aβ42*	Kan^r; for cytoplamically expression of Aβ42 from *E. coli*; used in the in vivo QM-FN-SO_3 fluorescence detection	This study
pET28b(+)-*hIAPP*	Kan^r; for periplasmically expression of hIAPP from E. *coli*; used in the in vivo QM-FN-SO_3 fluorescence detection	This study
pET28b(+)-*rIAPP*	Kan^r; for periplasmically expression of rIAPP from *E. coli*; used in the in vivo QM-FN-SO_3 fluorescence detection	This study
PCDFDuet-1	Strep^r Spec^r; vector only control; used in the in vivo QM-FN-SO_3 fluorescence detection	Lab stock
pCDFDuet-1-*ompX*	Strep^r Spec^r; for periplasmically expression of OmpX from *E. coli*; used in the in vivo QM-FN-SO_3 fluorescence detection	This study
pCDFDuet-1-*ompX-surA*	Strep^r Spec^r; for periplasmically co-expression of SurA and OmpX from *E. coli*; used in the in vivo QM-FN-SO_3 fluorescence detection	This study
pCDFDuet-1-*ompX-skp*	Strep^r Spec^r; for for periplasmically expression of Skp and OmpX from *E. coli*; used in the in vivo QM-FN-SO_3 fluorescence detection	This study

4.3 | Aggregate detection in vivo

Overnight cultures of BL21(DE3) expressing OmpX, Im7 wild type and mutants, MLL3 SET domain wild type and mutants, Aβ40, Aβ42, hIAPP, or rIAPP were inoculated into fresh LB culture containing 100 mg/mL kanamycin at a 1:100 dilution fold and cultured at 37°C, 220 rpm. When the $OD_{600\ nm}$ reached 0.5, 0.1 mM isopropyl-β-D-thiogalactoside (IPTG) was added to induce protein expression. At the indicated time, 1.5 OD cells were spun down and resuspended in 300 μL PBS buffer. Subsequently, 20 μM QM-FN-SO_3 was added and incubated for 20 min in a 37°C shaker to

allow the QM-FN-SO_3 probe to transverse the cell membrane and illuminate protein aggregates. Finally, the QM-FN-SO_3 fluorescent signals were measured with a fluorescence spectrometer or a microplate reader.

4.4 | Protein expression and purification

SurA, Skp, and OmpX were purified using previously established methods.[54,55] Briefly, 6×His-SUMO tagged SurA and Skp were initially purified by nickel affinity chromatography. The 6×His-SUMO tag was then removed by treatment with the ULP1 enzyme and the protein was further purified using ion-exchange chromatography on an ÄKTA system. For OmpX purification, protein aggregates in the cell pellet fraction were separated from the cell membrane fraction by washing with 20 mM Tris-HCl (pH = 8.5) buffer containing 5 mM EDTA and 2% Triton X-100 (v/v). The OmpX aggregates were subsequently solubilized in 20 mM Tris-HCl (pH = 8.5) with 5 mM EDTA and 8 M urea and were further purified by ion-exchange chromatography.

4.5 | Chaperone activity determination via the QM-FN-SO_3 probe

To test the ability of the QM-FN-SO_3 probe in characterizing chaperone activity in vitro, OmpX stock in 50 mM NaP, 100 mM NaCl, 8 M urea buffer (pH = 7.0) was diluted into a urea-free buffer supplemented with 1 μM QM-FN-SO_3 to a final concentration of 1.5 μM in the presence and absence of various concentrations of SurA or Skp. The QM-FN-SO_3 fluorescence signals and light scattering signals at 380 nm were monitored at 25°C respectively.

For chaperone activity assessment in vivo, we detected the aggregation levels of OmpX with and without co-expression of SurA or Skp in the periplasm of BL21(DE3) strains. Specifically, *ompX*, *surA*, and *skp* (all having their respective endogenous signal sequences) were cloned or co-cloned into a pCDFDuet vector and subsequently transformed into BL21(DE3) strains. After overnight cultivation, the strains harboring pCDFDuet-*ompX*, pCDFDuet-*ompX-surA*, or pCDFDuet-*ompX-skp* were transferred to fresh LB medium and allowed to grow at 37°C, 220 rpm. When the $OD_{600\ nm}$ reached 0.5, a final concentration of 0.1 mM IPTG was added to induce the corresponding protein expression. At the induction time of 0, 3, 6, 9, and 12 h, 1.5 OD cells of each strain were collected and used for aggregation detection by the QM-FN-SO_3 probe as described above.

4.6 | Fluorescence microscopy

1 OD cells of BL21(DE3) strains expressing OmpX (in the cytoplasm or periplasm, with and without co-expression chaperones), Aβ40, Aβ42, hIAPP, or rIAPP were spun down and resuspended in 500 μL PBS buffer containing 20 μM QM-FN-SO_3. After incubation for 10 min at 37°C, 5 μL of the cell suspension was transferred to a slide for fluorescence imaging. Super-resolution images were recorded using a structured light illumination microscopy (HiS-SIM) with a 488-nm laser and an Apo 100× oil objective, whereas conventional fluorescence images were recorded using a fluorescent inverted microscope (Nikon Eclipse Ti) with a 561-nm laser and an Apo 100× oil objective.

ACKNOWLEDGMENTS

This work was supported by the Natural Science Foundation of Shanghai, Grant Number: 23ZR1415300; The National Natural Science Foundation of China (NSFC), Grant Numbers: 32222049, 31661143021, 32171269, and 32201043; The National Key Research and Development Program of China, Grant Number: 2022YFF1102900; The Shanghai Frontier Science Center of Optogenetic Techniques for Cell Metabolism Shanghai Municipal Education Commission, Grant Number: 2021 Sci & Tech 03 28

CONFLICT OF INTEREST STATEMENT

The authors declare that there is no conflict of interest regarding the publication of this article.

DATA AVAILABILITY STATEMENT

The data used to support the findings of this study are included within the article and the supporting information.

ORCID

Wei He https://orcid.org/0000-0001-6263-5931
Shu Quan https://orcid.org/0000-0002-6672-4947

REFERENCES

1. C. Soto, S. Pritzkow, *Nat. Neurosci.* **2018**, *21*, 1332.
2. H. Olzscha, *Biol. Chem.* **2019**, *400*, 895.
3. D. Balchin, M. Hayer-Hartl, F. U. Hartl, *FEBS Lett.* **2020**, *594*, 2770.
4. D. Balchin, M. Hayer-Hartl, F. U. Hartl, *Science* **2016**, *353*, aac4354.
5. Y. E. Kim, M. S. Hipp, A. Bracher, M. Hayer-Hartl, F. U. Hartl, *Annu. Rev. Biochem.* **2013**, *82*, 323.
6. S. Horowitz, P. Koldewey, F. Stull, J. C. Bardwell, *Curr. Opin. Struct. Biol.* **2018**, *48*, 1.
7. F. U. Hartl, *Annu. Rev. Biochem.* **2017**, *86*, 21.
8. F. Chiti, C. M. Dobson, *Annu. Rev. Biochem.* **2017**, *86*, 27.
9. A. Kaushik, R. D. Jayant, S. Tiwari, A. Vashist, M. Nair, *Biosens. Bioelectron.* **2016**, *80*, 273.
10. Y. Zhang, G. Figueroa-Miranda, C. Zafiu, D. Willbold, A. Offenhäusser, D. Mayer, *ACS Sens.* **2019**, *4*, 3042.
11. S. S. Li, C. W. Lin, K. C. Wei, C. Y. Huang, P. H. Hsu, H. L. Liu, Y. J. Lu, S. C. Lin, H. W. Yang, C. C. Ma, *Sci. Rep.* **2016**, *6*, 25155.
12. Y. Zheng, L. Zhang, J. Zhao, L. Li, M. Wang, P. Gao, Q. Wang, X. Zhang, W. Wang, *Theranostics* **2022**, *12*, 2095.
13. Y. Zhang, B. Ren, D. Zhang, Y. Liu, M. Zhang, C. Zhao, J. Zheng, *J. Mater. Chem. B* **2020**, *8*, 6179.
14. A. Aliyan, N. P. Cook, A. A. Martí, *Chem. Rev.* **2019**, *119*, 11819.
15. D. Shen, Y. L. Bai, Y. Liu, *ChemBioChem* **2022**, *23*, e202100443.
16. M. M. Xu, W. M. Ren, X. C. Tang, Y. H. Hu, H. Y. Zhang, *Acta Pharmacol. Sin.* **2016**, *37*, 719.
17. M. G. Iadanza, M. P. Jackson, E. W. Hewitt, N. A. Ranson, S. E. Radford, *Nat. Rev. Mol. Cell Biol.* **2018**, *19*, 755.
18. M. R. Sawaya, M. P. Hughes, J. A. Rodriguez, R. Riek, D. S. Eisenberg, *Cell* **2021**, *184*, 4857.
19. Q. Xu, Y. Ma, Y. Sun, D. Li, X. Zhang, C. Liu, *Aggregate* **2023**, *4*, e333.
20. M. Groenning, *J. Chem. Biol.* **2010**, *3*, 1.
21. E. I. Yakupova, L. G. Bobyleva, I. M. Vikhlyantsev, A. G. Bobylev, *Biosci. Rep.* **2019**, *39*, BSR20181415.
22. Y. Tang, D. Zhang, Y. Zhang, Y. Liu, L. Cai, E. Plaster, J. Zheng, *J. Mater. Chem. B* **2022**, *10*, 2280.
23. Y. Zhou, J. Hua, D. Ding, Y. Tang, *Biomaterials* **2022**, *286*, 121605.
24. Y. Liu, C. H. Wolstenholme, G. C. Carter, H. Liu, H. Hu, L. S. Grainger, K. Miao, M. Fares, C. A. Hoelzel, H. P. Yennawar, G. Ning, M. Du, L. Bai, X. Li, X. Zhang, *J. Am. Chem. Soc.* **2018**, *140*, 7381.
25. B. Shen, K. H. Jung, S. Ye, C. A. Hoelzel, C. H. Wolstenholme, H. Huang, Y. Liu, X. Zhang, *Aggregate* **2022**, *4*, e239.

26. S. Ye, C. H. Hsiung, Y. Tang, X. Zhang, *Acc. Chem. Res.* **2022**, *55*, 381.
27. K. L. Zapadka, F. J. Becher, A. L. G. dos Santos, S. E. Jackson, *Interface Focus* **2017**, *7*, 20170030.
28. S. D. Stranks, H. Ecroyd, S. Van Sluyter, E. J. Waters, J. A. Carver, L. von Smekal, *Phys. Rev. E Stat. Nonlin. Soft Matter Phys.* **2009**, *80*, 051907.
29. Y. Yoshimura, Y. Lin, H. Yagi, Y. H. Lee, H. Kitayama, K. Sakurai, M. So, H. Ogi, H. Naiki, Y. Goto, *Proc. Natl. Acad. Sci. U. S. A.* **2012**, *109*, 14446.
30. P. Constantinescu, R. A. Brown, A. R. Wyatt, M. Ranson, M. R. Wilson, *J. Biol. Chem.* **2017**, *292*, 14425.
31. H. Jozawa, M. G. Kabir, T. Zako, M. Maeda, K. Chiba, Y. Kuroda, *FEBS Lett.* **2016**, *590*, 3501.
32. L. Breydo, J. W. Wu, V. N. Uversky, *Biochim. Biophys. Acta* **2012**, *1822*, 261.
33. D. Shen, W. Jin, Y. Bai, Y. Huang, H. Lyu, L. Zeng, M. Wang, Y. Tang, W. Wan, X. Dong, Z. Gao, H. L. Piao, X. Liu, Y. Liu, *Angew. Chem. Int. Ed.* **2021**, *60*, 16067.
34. W. Zhang, F. Huo, C. Yin, *J. Mater. Chem. B* **2018**, *6*, 6919.
35. W. Fu, C. Yan, Z. Guo, J. Zhang, H. Zhang, H. Tian, W. H. Zhu, *J. Am. Chem. Soc.* **2019**, *141*, 3171.
36. N. Chamachi, A. Hartmann, M. Q. Ma, A. Svirina, G. Krainer, M. Schlierf, *Proc. Natl. Acad. Sci. U. S. A.* **2022**, *119*, e2118919119.
37. B. Schiffrin, A. N. Calabrese, P. W. A. Devine, S. A. Harris, A. E. Ashcroft, D. J. Brockwell, S. E. Radford, *Nat. Struct. Mol. Biol.* **2016**, *23*, 786.
38. A. N. Calabrese, B. Schiffrin, M. Watson, T. K. Karamanos, M. Walko, J. R. Humes, J. E. Horne, P. White, A. J. Wilson, A. C. Kalli, R. Tuma, A. E. Ashcroft, D. J. Brockwell, S. E. Radford, *Nat. Commun.* **2020**, *11*, 2155.
39. S. E. Rollauer, M. A. Sooreshjani, N. Noinaj, S. K. Buchanan, *Philos. Trans. R. Soc. Lond. B Biol. Sci.* **2015**, *370*, 20150023.
40. J. G. Sklar, T. Wu, D. Kahne, T. J. Silhavy, *Genes Dev.* **2007**, *21*, 24 73.
41. X. Ge, R. Wang, J. Ma, Y. Liu, A. N. Ezemaduka, P. R. Chen, X. M. Fu, Z. Y. Chang, *FEBS J.* **2014**, *281*, 1226.
42. H. Kim, K. Wu, C. Lee, *Front. Mol. Biosci.* **2021**, *8*, 678697.
43. B. M. Burmann, S. Hiller, *Chimia* **2012**, *66*, 759.
44. V. Sachsenhauser, X. X. Deng, H. H. Kim, M. Jankovic, J. C. A. Bardwell, *ACS Chem. Biol.* **2020**, *15*, 1078.
45. C. Ren, X. Wen, J. Mencius, S. Quan, *Proc. Natl. Acad. Sci. U. S. A.* **2021**, *118*, e2101618118.
46. D. Chakraborty, J. E. Straub, D. Thirumalai, *Proc. Natl. Acad. Sci. U. S. A.* **2020**, *117*, 19926.
47. P. Nedumpully-Govindan, F. Ding, *Sci. Rep.* **2015**, *5*, 8240.
48. Y. Lin, H. Im, L. T. Diem, S. Ham, *Biochem. Biophys. Res. Commun.* **2019**, *510*, 442.
49. J. C. Saunders, L. M. Young, R. A. Mahood, M. P. Jackson, C. H. Revill, R. J. Foster, D. A. Smith, A. E. Ashcroft, D. J. Brockwell, S. E. Radford, *Nat. Chem. Biol.* **2016**, *12*, 94.
50. Y. Xu, R. Maya-Martinez, N. Guthertz, G. R. Heath, I. W. Manfield, A. L. Breeze, F. Sobott, R. Foster, S. E. Radford, *Nat. Commun.* **2022**, *13*, 1040.
51. G. Mas, J. Thoma, S. Hiller, *Subcell. Biochem.* **2019**, *92*, 169.
52. M. Kumar, Y. N. Hong, D. C. Thorn, H. Ecroyd, J. A. Carver, *Anal. Chem.* **2017**, *89*, 9322.
53. C. Yan, J. Dai, Y. Yao, W. Fu, H. Tian, W. H. Zhu, Z. Guo, *Nat. Protoc.* **2023**, *18*, 1316.
54. S. Quan, L. Wang, E. V. Petrotchenko, K. A. Makepeace, S. Horowitz, J. Yang, Y. Zhang, C. H. Borchers, J. C. Bardwell, *eLife* **2014**, *3*, e01584.
55. B. M. Burmann, C. Wang, S. Hiller, *Nat. Struct. Mol. Biol.* **2013**, *20*, 1265.
56. W. He, G. Yu, T. Li, L. Bai, Y. Yang, Z. Xue, Y. Pang, D. Reichmann, S. Hiller, L. He, M. Liu, S. Quan, *mBio* **2021**, *12*, e0213021.
57. W. He, J. Zhang, V. Sachsenhauser, L. Wang, J. C. A. Bardwell, S. Quan, *J. Biol. Chem.* **2020**, *295*, 14488.
58. Y. Li, J. Han, Y. Zhang, F. Cao, Z. Liu, S. Li, J. Wu, C. Hu, Y. Wang, J. Shuai, J. Chen, L. Cao, D. Li, P. Shi, C. Tian, J. Zhang, Y. Dou, G. Li, Y. Chen, M. Lei, *Nature* **2016**, *530*, 447.

SUPPORTING INFORMATION

Additional supporting information can be found online in the Supporting Information section at the end of this article.

How to cite this article: W. He, Y. Yang, Y. Qian, Z. Chen, Y. Zheng, W. Zhao, C. Yan, Z. Guo, S. Quan, *Aggregate* **2024**, *5,* e412.
https://doi.org/10.1002/agt2.412